

## AERODYNAMIC AND AEROTHERMODYNAMIC ASSESSMENT OF A LIFTING-BODY RE-ENTRY VEHICLE

Andrea Aprovitola, Nicolina Montella, Luigi Iuspa, Giuseppe Pezzella, and Antonio Viviani

University of Campania "L. Vanvitelli", Engineering Department. Via Roma 29, I-81031, Aversa (CE). Italy.

### Abstract

Future manned space missions and space tourism require safe and affordable re-entry from LEO orbit, intended even for an untrained crew. Considering the requirements of these missions, new re-entry technologies are currently being developed. This paper summarizes the research activities of the authors aimed at the preliminary Phase-A design of a configuration for a next generation reusable re-entry vehicle. The configuration design is performed using a multi-objective, multi-disciplinary optimization procedure consistent with an assigned set of requirements and constraints. An optimal conceptual configuration is then selected and frozen, and the Phase-A design is subsequently performed by using high-fidelity methods to assess design accuracy. Design is validated by processing computational fluid dynamics simulations at several specific points of the reentry trajectory to define the aerodynamic performance of the aircraft at the different speed regimes experienced during the descent. The aerothermal loading environment (*i.e.*, pressure loads and convective heat flux) is then determined by performing a single-target optimization, finding the best prescribed guidance law compatible with a rather constant heat flux profile.

**Keywords:** Reusable space vehicles; Re-entry aerodynamics; Multidisciplinary design optimization (MDO).

### 1. Introduction

The support service required by the International Space Station (ISS) demands reliable, high performance and reusable Crew Return Vehicles (CRV). Next generation CRVs shall replace capsules for crew rescue and transportation to and from the ISS. These vehicles should be able to perform a safe, comfortable (*i.e.*, with g-loads of unit order), and low turnaround re-entry on horizontal runway. For the same reason, sub-orbital space tourism will favor horizontal landings as only low g-loads can be tolerated to comply with high safety standards required for civilian passengers. Furthermore, next generation CRV demands significant weight reduction and, consequently, low aerothermal loads during re-entry, thus improving crew safety. Therefore, designers are currently focusing even more attention on non-conventional aeroshapes. Several examples of CRV lifting bodies are available in literature. For instance, the Northrop HL-10 was built from NASA to evaluate the aerodynamic performance of a so-called inverted airfoil configuration [1]. The HL-10 test bed was designed with a delta-planform lifting-body featuring three vertical planes, equipped with control surfaces [2]. HOPE-X is another example of Shuttle-like spacecraft [3]. A 25% scale model of HOPE-X was released at an altitude of 20–30 km, by a stratospheric balloon, performing different maneuvers during experimental flight tests [4], [5]. Similar tests drove to FALKE program aimed at flying a sub-scale model of the Space Shuttle orbiter in real conditions [6]. The NASA HL-20 project resumes American efforts for the design of a crew emergency vehicle for ISS, notably for crew rescue back to Earth [3]. Longitudinal maneuverability is allowed by two body flaps at fuselage trailing edge, while two canted fins are mounted on the aft portion of the model for lateral-directional control [7], [8]. Two main projects represent European efforts toward the experimental high-lift flight activities carried out in the preparation of future space programs, namely Phoenix and IXV [9], [10]. The IXV vehicle was developed by ESA to test maneuvering capabilities of a lifting body within a typical LEO re-entry environment. As far as United States efforts are concerned, it is worth mentioning the Boeing X-37B

and the Dream Chaser. the former (*i.e.*, the Boeing X-37B) is an unmanned winged vehicle currently operative that is the only one that re-enters from space, thus performing a horizontal landing on runway [8].

Finally, the Dream Chaser, developed by SNC, features a lifting-body aeroshape with small wings. This spacecraft is one of the most interesting design candidates developed so far for a CRV. It allows gliding, banking, and landing to assigned conventional runways due to its very interesting aerodynamic and aerothermodynamic performances.

In this work, a small-sized optimized Blended Wing Body (BWB) aeroshape, with fuselage and wing seamlessly integrated in a delta-shaped planform, is investigated throughout the whole re-entry flight, from hypersonic down to subsonic regimes. The spacecraft three-view drawing is provided in Figure 1. As one can see, the aeroshape features a monolithic wing-body configuration with a double-delta wing planform characterized by a low aspect ratio and bent rounded wing tips. It also shows a flat-bottomed belly side with wing dihedral angle, and a nose drop-down forebody. These aeroshape features satisfy the conflicting requirements represented by a design compromise between a blunt configuration (favoring heat dissipation and drag deceleration), and a lifting configuration with aircraft-like capabilities allowing levelled flight at higher altitude and safe landing on conventional runways.

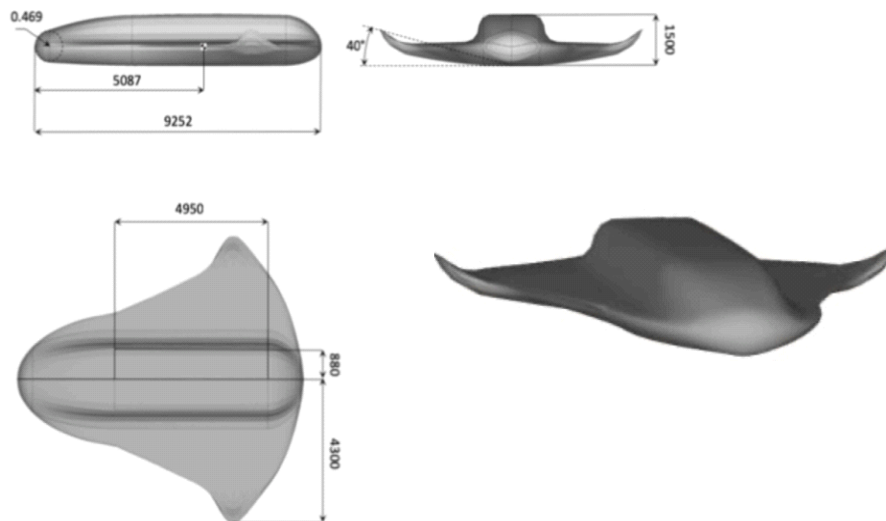


Figure 1 - Three-views drawings.

A pictorial representation of the spacecraft close to the ISS is reported in Figure 1.



Figure 2 - A pictorial representation of the re-entry vehicle close to the ISS.

As discussed in Ref. [11], a prescribed guidance law was found to allow a more gradual conversion of spacecraft energy into heat by increasing the duration of the re-entry flight.

In particular, the optimization procedure developed in Ref. [11] was able to find a spacecraft trajectory that, for the given aeroshape configuration and an assigned heat flux level, ensures a rather constant convective heat flux profile at the CRV stagnation point as long as possible.

This allows to reduce convective peak heat flux and, at the same time, gives the possibility to customize the landing spot. Further, a gentler aerothermal environment allows the adoption of lightweight reusable heatshields, which exploits thermal radiation cooling with no ablation phenomena. Therefore, the spacecraft should benefit of a short refurbishment time for a low turnaround mission rate.

This framework points out that the CRV design must satisfy a complex framework which relates safety, operability, structural and aerodynamic constraints, cost reduction, and finally, flight comfort [4]. The above-mentioned demands can be accounted by exploiting a Multi-disciplinary Design Optimization (MDO) procedure. Usually, a parametric shape generator efficiently supports a chain of sub-discipline analyses linked to an optimization procedure, often performed with evolutionary algorithm (*i.e.*, Genetic Algorithm, GA) [12], [13], [14].

In this framework, the paper explores two phases devoted to a design synthesis of a new spacecraft candidate for a return mission from Low Earth orbit (LEO), able to perform a landing on a conventional runway. Specifically, MDO is first adopted to determine design candidate configurations which adhere to a set of mission constraints. Furthermore, the support of Computational Fluid Dynamics (CFD) simulations to design synthesis is shown to refine the aerodynamics of the Phase-A compliant configuration.

## 2. Mission requirements, constraints and aeroshape conceptual design

### 2.1 Mission requirements

The reference mission requirement dictates that the concept aeroshape shall be put into LEO orbit by a launcher, dock or undock on/from the ISS and perform an Earth re-entry in both manned and unmanned configuration. The CRV can be used either as emergency vehicle or simply as return vehicle for four astronauts crew turnover on the ISS.

### 2.2 Mission constraints

Fly-back mission starts at entry interface at altitude and speed set equal to 120 Km and 7830 m/s, respectively. The floor of the re-entry corridor refers to maximum heat flux limit equal to 760 kW/m<sup>2</sup>, maximum dynamic pressure of 14 kPa, and maximum normal load factor of 2.5 g (Figure 3).

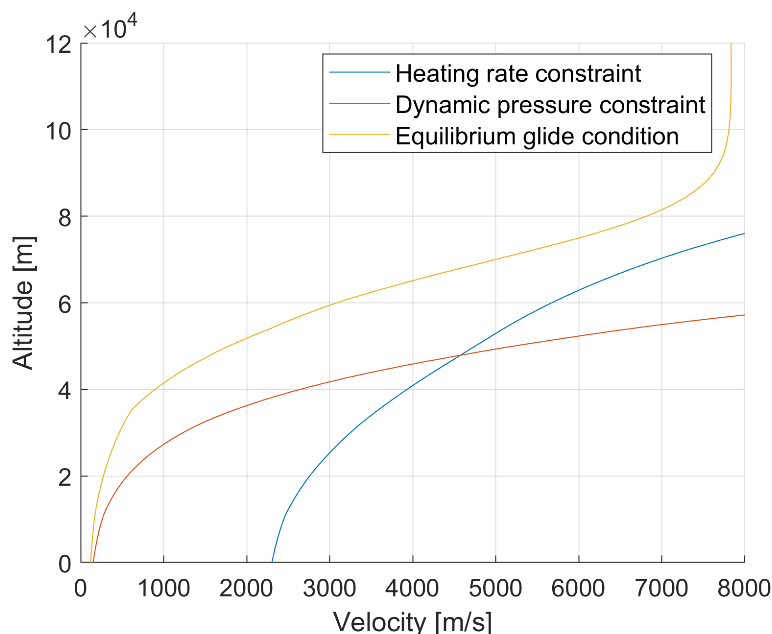


Figure 3 - Re-entry corridor.

Then, the maximum landing speed ( $V_{\max}$ ) is 110 m/s.

The initial re-entry AoA,  $\alpha_{\text{opt}}$ , is constrained to be within the range  $[35^\circ, 50^\circ]$ . The bank angle is assumed as a design variable, and its value can be chosen between the range  $[-50^\circ, 50^\circ]$ , but no modulation of  $\mu_a$  is allowed, *i.e.*, that value remains constant during the re-entry.

### 2.3 Aeroshape design

The aeroshape is found according to the design structure matrix (DSM), shown in Figure 4.

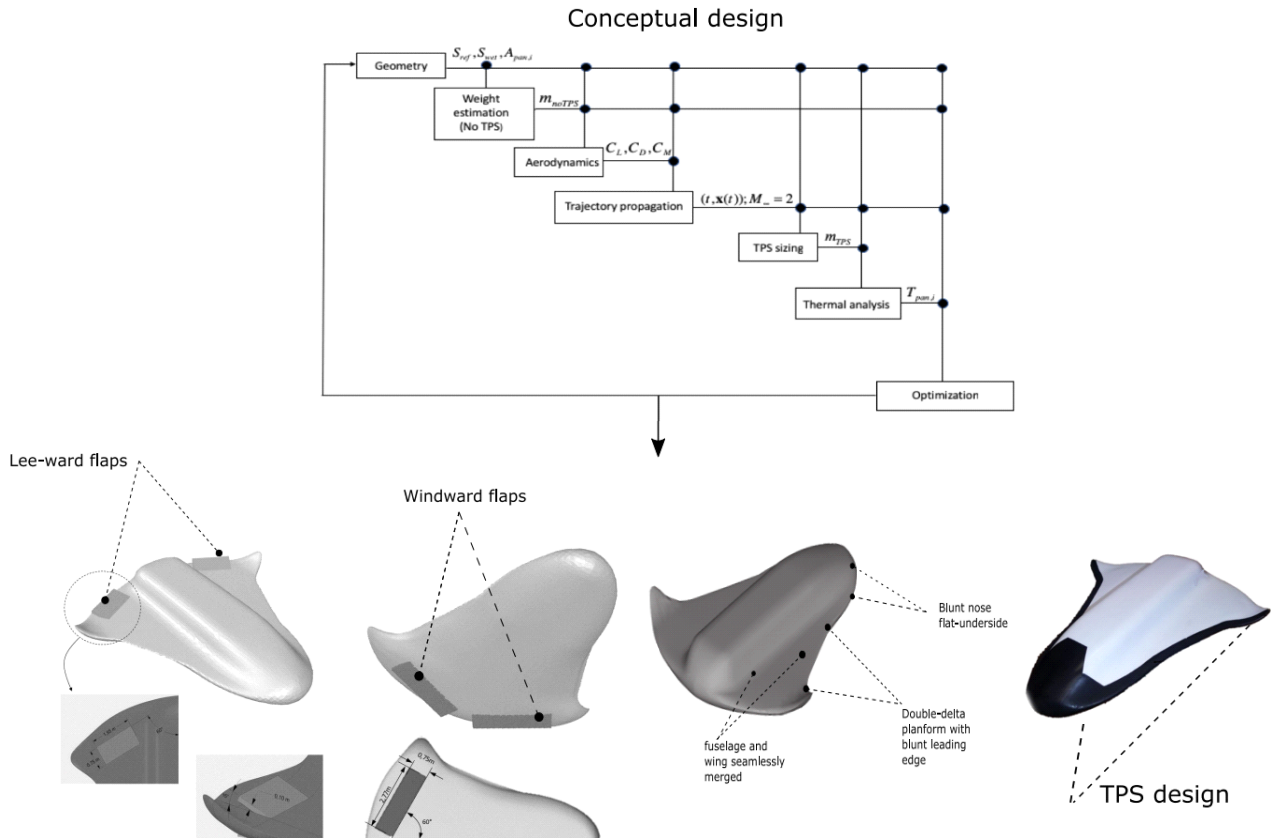


Figure 4 - Spacecraft DSM.

In Figure 4, several steps of the design framework are regrouped. In the first step, an optimization procedure is used to select and build from scratch a candidate conceptual configuration.

The MDO procedure performs explorative evaluations of the configuration in the search space defined by a state vector composed by geometric, aero-thermodynamic, and flight dynamics suggestions [15]. In the conceptual phase, aerodynamic coefficients are computed with multi-regime Panel Methods (PMs), *i.e.*, potential flow panel for subsonic speeds and Newtonian surface inclination panel methods for hypersonic speeds.

Furthermore, several simplifying assumptions made in the early stages of design are progressively removed.

Once a best candidate has been selected, the aeroshape configuration is frozen.

Phase-A design accuracy is addressed by means of several CFD simulations that are performed and used to assembly an accurate test matrix which refines the vehicle re-entry corridor. For instance, the longitudinal stability margin at hypersonic and supersonic speeds are obtained by CFD computations, as detailed in Ref. [16].

Moreover, a low-speed evaluation of vehicle Aerodynamics at landing incidence is also performed in pre/post-stall conditions to evaluate efficiency of the preliminary configuration, as discussed in Ref. [16] and Ref. [17].

A feasible, non-dominated candidate aeroshape, resulting from the MDO investigation, features 9.25 m as total length; 1.5 m as total height; 8.6 m as wingspan; 0.469 m as nose radius; 40° as bent angle, as shown in Figure 1.

Mass budget provided the following estimations: 36% for structure and mechanisms, 43% for subsystems, 17% for TPS, and 4% for crew for an overall mass  $m_{tot}=12105$  kg.

See Ref. [15-19], [11] for further details.

Subsequently, a prescribed optimal Guidance Law (GL), expressed as a functional relation between the AoA  $\alpha$ , and the Mach number  $M_\infty$ , is derived using a single objective optimization procedure.

The objective function of the GL optimization problem is formulated by considering that a trajectory producing a rather constant heat flux profile at the spacecraft stagnation point has to lie on the re-entry corridor thermal constraint curve.

This goal must be satisfied without overcome the dynamic pressure constraint [11].

### 3. Vehicle Aerodynamics and Aerothermodynamics

#### 3.1 High-speed aerodynamic performances

Phase-A aerodynamics of the CRV at hypersonic speeds relies on a large number of engineering-based evaluations carried out with Newtonian PMs (*i.e.*, surface inclinations methods).

An aerodynamic test-matrix considered for PM evaluations regroups flight conditions individuated by  $(\alpha, M_\infty)$  values given by envelope of the arrays:  $M_\infty = [2:25]$  and  $\alpha = [0: 45^\circ]$ .

More reliable numerical flowfield computations have been carried out with CFD simulations for some specific flight conditions extracted by the test-matrix, with and without taking into account for high-temperature real gas effects, typical of flight conditions at very high Mach numbers.

A summary of the CRV high-Mach numbers clean configuration aerodynamics is provided in both Figure 5 and Table 1.

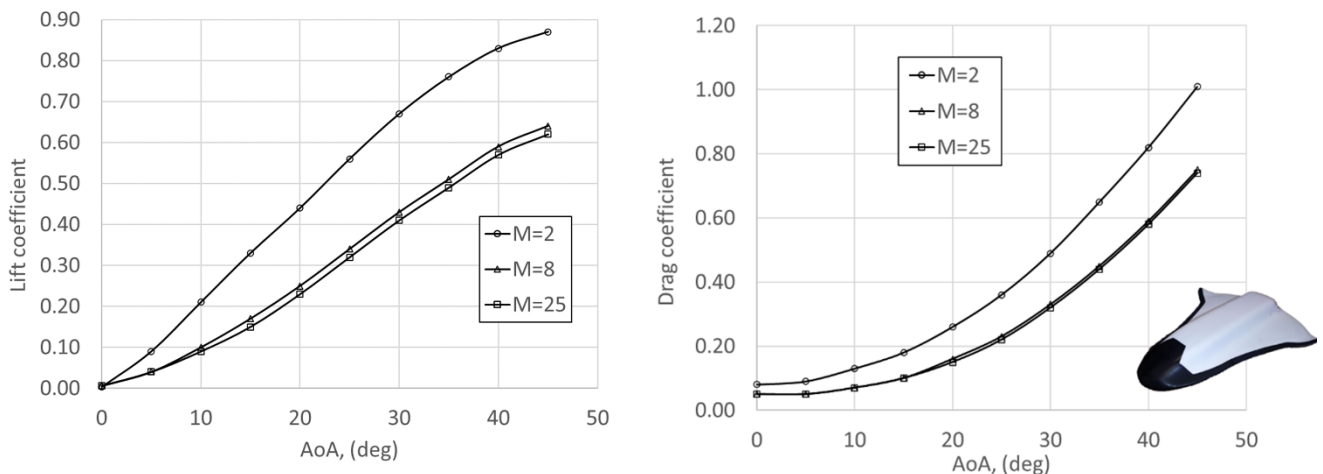


Figure 5 - CRV high-Mach numbers clean configuration aerodynamics.

| AoA, deg | Mach                                  |        |        |        |        |        |        |        |
|----------|---------------------------------------|--------|--------|--------|--------|--------|--------|--------|
|          | 2                                     | 4      | 6      | 8      | 10     | 15     | 20     | 25     |
|          | Lift coefficient, $C_L$               |        |        |        |        |        |        |        |
| 0        | 0.003                                 | 0.003  | 0.005  | 0.006  | 0.006  | 0.006  | 0.006  | 0.006  |
| 5        | 0.090                                 | 0.060  | 0.050  | 0.040  | 0.040  | 0.040  | 0.040  | 0.040  |
| 10       | 0.210                                 | 0.130  | 0.110  | 0.100  | 0.090  | 0.090  | 0.090  | 0.090  |
| 15       | 0.330                                 | 0.210  | 0.180  | 0.170  | 0.160  | 0.160  | 0.150  | 0.150  |
| 20       | 0.440                                 | 0.300  | 0.260  | 0.250  | 0.240  | 0.230  | 0.230  | 0.230  |
| 25       | 0.560                                 | 0.390  | 0.350  | 0.340  | 0.330  | 0.320  | 0.320  | 0.320  |
| 30       | 0.670                                 | 0.480  | 0.440  | 0.430  | 0.420  | 0.410  | 0.410  | 0.410  |
| 35       | 0.760                                 | 0.570  | 0.530  | 0.510  | 0.500  | 0.500  | 0.500  | 0.490  |
| 40       | 0.830                                 | 0.640  | 0.610  | 0.590  | 0.580  | 0.570  | 0.570  | 0.570  |
| 45       | 0.870                                 | 0.690  | 0.650  | 0.640  | 0.630  | 0.630  | 0.630  | 0.620  |
|          |                                       |        |        |        |        |        |        |        |
|          | Drag coefficient, $C_D$               |        |        |        |        |        |        |        |
| 0        | 0.080                                 | 0.060  | 0.050  | 0.050  | 0.050  | 0.050  | 0.050  | 0.050  |
| 5        | 0.090                                 | 0.060  | 0.060  | 0.050  | 0.050  | 0.050  | 0.050  | 0.050  |
| 10       | 0.130                                 | 0.090  | 0.080  | 0.070  | 0.070  | 0.070  | 0.070  | 0.070  |
| 15       | 0.180                                 | 0.120  | 0.110  | 0.170  | 0.100  | 0.100  | 0.100  | 0.100  |
| 20       | 0.260                                 | 0.180  | 0.170  | 0.160  | 0.160  | 0.150  | 0.150  | 0.150  |
| 25       | 0.360                                 | 0.260  | 0.240  | 0.230  | 0.230  | 0.220  | 0.220  | 0.220  |
| 30       | 0.490                                 | 0.370  | 0.340  | 0.330  | 0.330  | 0.320  | 0.320  | 0.320  |
| 35       | 0.650                                 | 0.500  | 0.460  | 0.450  | 0.450  | 0.440  | 0.440  | 0.440  |
| 40       | 0.820                                 | 0.640  | 0.610  | 0.590  | 0.590  | 0.580  | 0.580  | 0.580  |
| 45       | 1.010                                 | 0.810  | 0.770  | 0.750  | 0.750  | 0.740  | 0.740  | 0.740  |
|          |                                       |        |        |        |        |        |        |        |
|          | Pitching moment coefficient, $C_{M0}$ |        |        |        |        |        |        |        |
| 0        | 0.003                                 | -0.005 | -0.007 | -0.008 | -0.008 | -0.093 | -0.009 | -0.009 |
| 5        | -0.092                                | -0.055 | -0.045 | -0.041 | -0.038 | -0.034 | -0.033 | -0.032 |
| 10       | -0.195                                | -0.115 | -0.094 | -0.084 | -0.079 | -0.073 | -0.071 | -0.072 |
| 15       | -0.305                                | -0.188 | -0.157 | -0.144 | -0.137 | -0.13  | -0.128 | -0.127 |
| 20       | -0.421                                | -0.272 | -0.235 | -0.221 | -0.213 | -0.205 | -0.202 | -0.201 |
| 25       | -0.547                                | -0.37  | -0.329 | -0.312 | -0.305 | -0.297 | -0.294 | -0.293 |
| 30       | -0.686                                | -0.481 | -0.436 | -0.421 | -0.412 | -0.404 | -0.401 | -0.399 |
| 35       | -0.819                                | -0.603 | -0.556 | -0.534 | -0.53  | -0.522 | -0.519 | -0.518 |
| 40       | -0.961                                | -0.732 | -0.684 | -0.668 | -0.659 | -0.65  | -0.647 | -0.646 |
| 45       | -1.105                                | -0.866 | -0.817 | -0.801 | -0.791 | -0.783 | -0.78  | -0.778 |

Table 1 – High-Mach numbers clean configuration aerodynamics.

Further details about high-speed aerodynamics can be found in Ref. [15] and Ref. [22].

### 3.2 Low-speed aerodynamic performances

Aerodynamic performance at low speed is carried out up to  $M_\infty=0.3$ , that is the conventional threshold which divides incompressible to compressible flows [20-22]. The maximum allowable landing speed is assumed equal to 110 m/s. Aerodynamic analyses performed at subsonic speed pointed out that the BWB aeroshape with a delta planform wing conforms to the mission requirements and constraints.

Furthermore, the current design also allows an efficient integration of body-flaps which improves vehicle control, trim and aerodynamic performances, especially for the landing phase.

In the proposed layout, body-flaps can be used either as elevon (*i.e.*, symmetric deflections) or as ailerons (*i.e.*, asymmetric deflections), see Figure 4.

A summary of the CRV low-Mach numbers clean configuration aerodynamics is provided in both Figure 6 and Table 2.

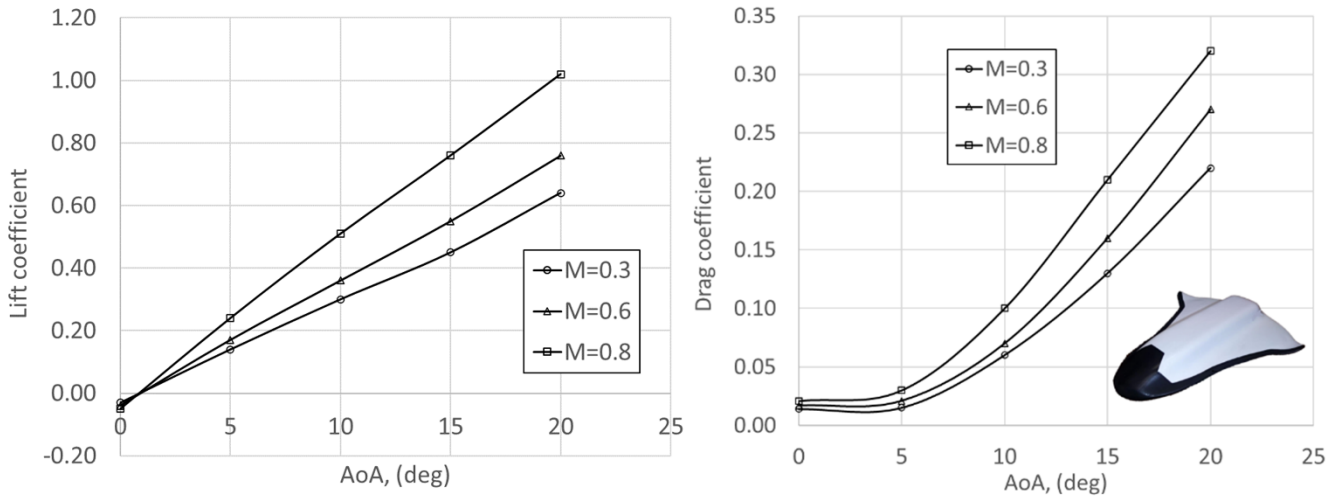


Figure 6 – CRV low-Mach numbers clean configuration aerodynamics.

|          | Mach                                  |        |        |        |
|----------|---------------------------------------|--------|--------|--------|
|          | 0.3                                   | 0.4    | 0.6    | 0.8    |
| AoA, deg | Lift coefficient, $C_L$               |        |        |        |
| 0        | -0.03                                 | -0.03  | -0.04  | -0.05  |
| 5        | 0.14                                  | 0.12   | 0.17   | 0.24   |
| 10       | 0.3                                   | 0.31   | 0.36   | 0.51   |
| 15       | 0.45                                  | 0.48   | 0.55   | 0.76   |
| 20       | 0.64                                  | 0.66   | 0.76   | 1.02   |
| AoA, deg | Drag coefficient, $C_D$               |        |        |        |
| 0        | 0.014                                 | 0.015  | 0.017  | 0.021  |
| 5        | 0.015                                 | 0.014  | 0.021  | 0.030  |
| 10       | 0.060                                 | 0.060  | 0.070  | 0.100  |
| 15       | 0.130                                 | 0.140  | 0.160  | 0.210  |
| 20       | 0.220                                 | 0.230  | 0.270  | 0.320  |
| AoA, deg | Pitching moment coefficient, $C_{M0}$ |        |        |        |
| 0        | 0.020                                 | 0.022  | 0.025  | 0.033  |
| 5        | -0.070                                | -0.076 | -0.088 | -0.117 |
| 10       | -0.188                                | -0.205 | -0.235 | -0.313 |
| 15       | -0.298                                | -0.325 | -0.373 | -0.497 |
| 20       | -0.440                                | -0.480 | -0.550 | -0.733 |

Table 2 – Low-Mach number clean configuration aerodynamics.

Further details about low-speed aerodynamics, such as aerodynamic control surfaces effectiveness, can be found in Ref. [16] and Ref. [23].

### 3.3 Aerothermodynamic performances

Aeroheating analysis is fundamental for the design of the Thermal Protection System (TPS) of the CRV. In fact, the re-entry aerothermal loading environment determines the TPS thickness and the choice of insulating materials of the vehicle heatshield [24], [25]. According to Szirczak et al. [26], next generation re-entry gliders will adopt a lightweight (passive), fully reusable TPS to withstand

several flights without any replacement.

Recall that, the TPS sizing relies on the peak heating and the time-integrated thermal load which, in turn, can be computed once the re-entry trajectory is available [27].

Surface distributions of convective heat flux ( $\dot{q}$ ) are determined using kinematic trajectory data in the range  $2 \leq M_\infty \leq 23$ , where heat flux peaks are expected to occur. For instance, an example of the aerothermal loading environment expected for the CRV are provided in Figure 7-b. This profile of  $\dot{q}$  is the convective heat flux expected at the stagnation point of the CRV while flying the corresponding re-entry trajectories reported in Figure 7-a.

For the sake of simplicity, according to a preliminary design phase, several complex heat transfer effects, like e.g. catalytic recombination, low density effects, and thermal radiation from spacecraft non-convex surfaces, are neglected. As shown, the aerothermal loading environment is strictly related to re-entry flight.

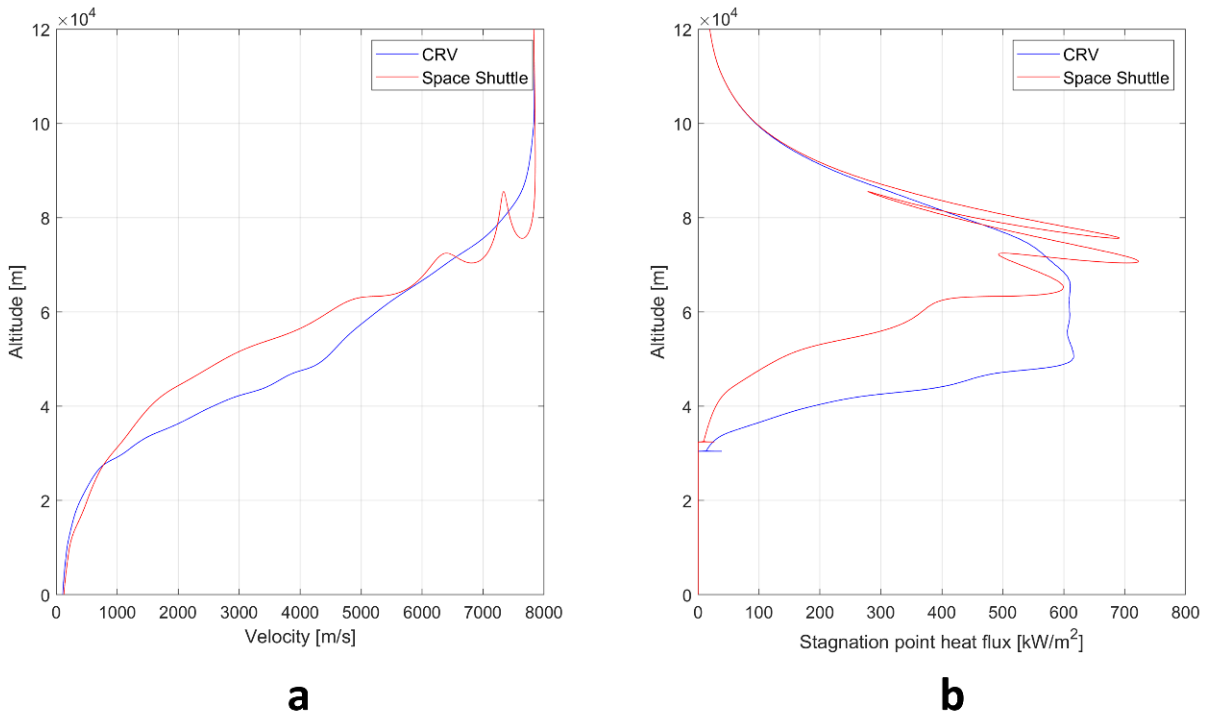


Figure 7 a-b – Comparison between Shuttle-like GL re-entry trajectory and CRV admissible re-entry trajectory: Re-entry trajectory vs. altitude (a); Stagnation point heat flux vs. altitude (b).

As discussed in Ref. [11] and [13], different re-entry flight profiles of the CRV are possible according to a prescribed GL. For instance, Figure 7-a shows a re-entry trajectory corresponding to a Shuttle-like GL, *i.e.*, a prescribed piecewise linear angle of attack (AoA) profile followed by the spacecraft during descent.

According to Figure 7-a, this trajectory exhibits several oscillations during the hypersonic phase; this behavior should be avoided to preserve thermal efficiency of the heatshield.

In fact, heat flux peaks (Figure 7-b) correspond to those trajectory sinks, causing several cycles of vehicle over-heating followed by cooling phases. Therefore, as discussed in Ref. [18], an optimization problem is formulated to search the optimal prescribed GL, expressed as a ( $\alpha$ ,  $M_\infty$ ) modulation, able to provide a rather constant heat flux profile as longer as possible in the high-speed range.

A target figure represented by a maximum convective heat flux of 600 kW/m<sup>2</sup>, which represents the floor of the re-entry corridor, is assigned, and initial entry conditions are given assuming:  $V_e = 7830$  m/s,  $\gamma_0 = -0.1^\circ$  to perform a shallow re-entry and reduce the drag-acceleration obtaining a constant value of heat flux in the most significant region of the re-entry corridor. The target convective heat flux is subsequently reduced as more as possible to ensure a safety margin on the peaks, as described in Ref. [11].

This shows that it is possible to have a rather constant heat flux profile at the CRV stagnation point for the aeroshape in Figure 1 keeping a safety margin on the convective heat flux peaks over the maximum target not higher than about 10%.

As shown in Figure 7-a, the optimization provided a re-entry trajectory that does not feature the phugoid behavior, typical of the shuttle-like skip re-entry.

Furthermore, in the altitude range between (80–60) km, which corresponds to a speed range of (4000 – 6200) m/s, the heat flux matches the prescribed target value. As said before, a constant heat flux peak at the stagnation point assures a safer re-entry for lightweight thermal protection materials.

#### 4. Conclusions

The paper dealt with a design procedure for a CRV vehicle aimed at performing a LEO return mission, which ends with a landing on a conventional runway. A multi-objective optimization procedure was used to find the CRV preliminary design.

Numerical simulations have been addressed to anchor and provide engineering-based design results and fundamental insights on several design items, such as spacecraft aerodynamics and aerothermodynamics.

The aerodynamic performances of the optimized spacecraft have proven that the vehicle is able to perform a trajectory characterized by a rather constant convective heat flux with a constraint value of 600 kW/m<sup>2</sup>. It also has been shown the capability to land on a conventional runway at a touchdown speed below about 110 m/s, compatible with the structural limits of the landing gear.

#### 5. Contact Author Email Address

Author e-mail address for future contacts is: [giuseppe.pezzella@unicampania.it](mailto:giuseppe.pezzella@unicampania.it)

#### 6. Copyright Statement

The authors confirm that they, and/or their company or organization, hold copyright on all of the original material included in this paper. The authors also confirm that they have obtained permission, from the copyright holder of any third party material included in this paper, to publish it as part of their paper. The authors confirm that they give permission, or have obtained permission from the copyright holder of this paper, for the publication and distribution of this paper as part of the ICAS proceedings or as individual off-prints from the proceedings.

#### References

- [1] Kempel R W, Painter W D and Thompson M O. Developing and flight testing the HL-10 lifting body: A precursor to the space Shuttle. NASA reference publication 1332, 1994
- [2] Reed Dale R, and Lister D. Wingless Flight: The Lifting Body Story. University Press of Kentucky, 2002, ISBN 0-8131-9026-6.
- [3] Venel S, Fauncon P, Yanagihara M, Miyazawa Y, Akimoto T, and Sagisaka, M. Hope-X high speed flight demonstration program phase II –a CNES/NAL/NASDA cooperation. Advances in space research, 35, 1613–1616, 2003.
- [4] Marley C D, Driscoll J F. Modeling an Active and Passive Thermal Protection System for a Hypersonic Vehicle. AIAA SciTech Forum 9-13 January, Grapevine, Texas.
- [5] Yanagihara M, Miyazawa Y, Munenaga T, Venel S, Guedron S, and Cretenet J C Results of high-speed flight demonstration phase II. Space Technology, 2005, 25(1), 37–50.
- [6] Radespiel R. Subsonic Flow Around US-Orbiter Model FALKE in the DNW. AGARD Advisory Report No. 303, 1994.
- [7] NASA, Human Space Flight. Simulating Dream Chaser Spacecraft Aerodynamics: Subsonic through Hypersonic. 2020, <https://www.nas.nasa.gov/SC19/demos/demo1.html#prettyPhoto>.
- [8] Szirczak D and Smith H. A review of design issues specific to hypersonic flight vehicles. Progress in Aerospace Sciences, 84, 1-28, 2016.
- [9] Tumino D and Angelino E and Leleu F, Angelini R and Plotard P and Sommer J. The ESA Re-Entry System and Technologies Demonstrator Paving the Way to European Autonomous Space Transportation and Exploration Endeavours. 59<sup>th</sup> International Astronautical Congress. IAC 2008. Glasgow, United Kingdom IAC 2008. Glasgow, United Kingdom.
- [10] Jategaonkar R and Behr R and Gockel W and Zorn C. Flight demonstrator concept for key technologies enabling future reusable vehicles. AIAA Atmospheric Flight Mechanics Conference and Exhibition, 15-18 August 2005, San

## AERODYNAMIC AND AEROTHERMODYNAMIC ASSESSMENT OF A LIFTING-BODY RE-ENTRY VEHICLE

Francisco, California.

- [11] Montella N, Aprovitola A, Iuspa L, and Pezzella G. Aeroshape and Trajectory Design of Next Generation Re-Entry Vehicles. 33<sup>rd</sup> Congress of the International Council of the Aeronautical Sciences. Stockholm, Sweden, 4-9 September 2022.
- [12] Dirkx D and Mooij E. Optimization of entry-vehicle shapes during conceptual design. *Acta Astronautica*, 94(1) (2014) 198-214.
- [13] Tava M and Suzuki S. Multidisciplinary Design Optimization of a Re-Entry Vehicle Shape and Trajectory. AIAA Paper 2001-28095, 2001.
- [14] Lobbia M A. Multidisciplinary Design Optimization of Waverider-Derived Crew Reentry Vehicles. *Journal of Spacecraft and Rockets*, 54 (1) (2017) 233-245.
- [15] Viviani A, Iuspa L, Aprovitola A. Multi-objective Optimization for Re-entry Spacecraft Conceptual Design Using a Free-form Shape Generator. *Aerospace Science and Technology*, 71, 312-324, 2017.
- [16] Viviani A, Iuspa L, Aprovitola A, Pezzella G. Aeroshape design of reusable re-entry vehicles by multidisciplinary optimization and computational fluid dynamics. *Aerospace Science and Technology*, 105, 2020.
- [17] Viviani A, Aprovitola A, Pezzella G. Low Speed Longitudinal Aerodynamics of a Blended Wing-Body Re-Entry Vehicle. *Aerospace Science and Technology*, 107, 2020.
- [18] Aprovitola A, Montella N, Iuspa L, Pezzella G, Viviani A. An optimal heat-flux targeting procedure for LEO re-entry of reusable vehicles. *Aerospace Science and Technology*, Volume 112, May 2021.
- [19] Aprovitola A, Iuspa L, Viviani A. Thermal protection system design of a reusable launch vehicle using integral soft objects. *International Journal of Aerospace Engineering*, 2019.
- [20] ANSYS Fluent User's Guide.
- [21] Bucchignani E and Pezzella G. Computational flowfield analyses of hypersonic problems with reacting boundary layer. *Mathematics and Computers in Simulation*, 81 (3), 656-669, 2010.
- [22] Viviani A, Pezzella G and Golia C. Effects of thermochemical modelling and surface catalyticity on an Earth re-entry vehicle. *Proceedings of the Institution of Mechanical Engineers, Part G: Journal of Aerospace Engineering*, 225 (5), 523-540, 2011.
- [23] Aprovitola A, Iuspa L, Pezzella G, and Viviani A. Optimal Design of a Next Generation High-Lift Reusable Re-Entry Vehicle. 32<sup>nd</sup> Congress of the International Council of the Aeronautical Sciences. Shanghai, China, 6-10 September 2021.
- [24] Kumar S, and Mahulikar S. P. Design of thermal protection system for reusable hypersonic vehicle using inverse approach. *Journal of Spacecraft and Rockets*, 54(2):436– 446, 2017.
- [25] Olynick D. Trajectory-based thermal protection system sizing for an X-33 winged vehicle concept. *Journal of Spacecraft and Rockets*, 35(3):249–2566, 2017.
- [26] Szirczak D. and Smith H. A review of design issues specific to hypersonic flight vehicles. *Progress in Aerospace Sciences*, 84:1–28, 2016.
- [27] Mazzaracchio A. Thermal protection system and trajectory optimization for orbital plane change aeroassisted maneuver. *Journal of Aerospace Technology*, 5(1):49–64, 2013